Ground-Based Hyperspectral Image Surveillance System for Explosive Detection: Methods, Experiments, and Comparisons

Mustafa Kütük, İzlen Geneci, Okan Bilge Özdemir, Alper Koz, Okan Esentürk, Yasemin Yardımcı Çetin, and A. Aydın Alatan

***Abstract*—Explosive detection is crucial for public safety and confidence. Among various solutions for this purpose, hyperspectral imaging differs from its alternatives with its detection capability from standoff distances. However, the state-of-the-art for such a technology is still significantly missing a complete technical and experimental framework for surveillance applications. In this article, an end-to-end technical framework, which involves capturing, preprocessing, reflectance conversion, target detection, and performance evaluation stages, is proposed to reveal the potential of a ground-based hyperspectral image (HSI) surveillance system for the detection of explosive traces. The proposed framework utilizes a short-wave infrared region (0.9–1.7 μm), which covers the distinctive absorption characteristics of different explosives. Three classes of detection methods, namely index, signature, and learning-based methods are adapted to the proposed surveillance system. Their performances are compared over various experiments, which are specifically designed for granular and sprayed residues, fingerprint residues, and explosive traces on vehicles. The experiments reveal that the best method in terms of precision and recall performances is hybrid structure detector, which effectively combines signature-based detection with unmixing. While deep-learning-based methods have also achieved satisfactory precision values, their low recall values for the moment have comparatively limited their usage for the high-risk cases. Although one of the main reasons for the current performances of deep-learning methods is less data for learning, these performances for HSIs can be increased with more data in the future as in other image applications.**

***Index Terms*—Deep learning, explosive detection, hybrid structure detection (HSD), hyperspectral image (HSI) surveillance, index-based methods, learning-based methods, signature-based target detection algorithms.**

Manuscript received 11 April 2023; revised 10 June 2023 and 6 July 2023; accepted 14 July 2023. Date of publication 28 July 2023; date of current version 28 September 2023. This work was supported by the Havelsan Teknoloji Radar San. ve Tic. Inc., Turkey. *(Corresponding author: Mustafa Kütük.)*

Mustafa Kütük, İzlen Geneci, Okan Bilge Özdemir, and Alper Koz are with the Center for Image Analysis, Middle East Technical University, 06800 Ankara, Turkey (e-mail: mkutuk@metu.edu.tr; izlen.geneci@metu.edu.tr; oozdemir@metu.edu.tr; koz@metu.edu.tr).

Okan Esentürk is with the Department of Chemistry, Middle East Technical University, 06800 Ankara, Turkey (e-mail: eokan@metu.edu.tr).

Yasemin Yardımcı Çetin is with the Informatics Institute, Middle East Technical University, 06800 Ankara, Turkey (e-mail: yyardim@metu.edu.tr).

A. Aydın Alatan is with the Center for Image Analysis and Department of Electrical and Electronics Engineering, Middle East Technical University, 06800 Ankara, Turkey (e-mail: alatan@metu.edu.tr).

Digital Object Identifier 10.1109/JSTARS.2023.3299730

I. Introduction

DETECTION of explosive materials and their traces [1], [2], [3], [4], [5] has been an increasingly important research field for long years due to the endless conflicts on a global scale in many different parts of the world. Hyperspectral imaging (HSI) is one of the potential solutions for such an aim with its distinctive capability for standoff detection in contrary to the commonly utilized techniques in state-controlled points, such as X-ray diffraction imaging and differential mobility spectrometry [6], [7]. However, the widespread utilization of this developing technology for public safety with broader surveillance applications still involves various research challenges regarding the target detection methods, design of the experiments, registration and regulation of spectral bands for the construction of hyperspectral cubes in dynamic scenes, and acquisition speeds for moving targets including vehicles and people. Among these challenges, this article focuses on the detection methods for explosive materials and the design of experiments for varying real case scenarios to reveal the performance of these methods.

The HSI studies for explosive detection are mainly based on the comparison of the reflectance or emissivity spectrum of the tested HSI pixel and the reference spectrum of the target explosive. These studies first capture the reflected radiance spectra in a scene in multiple successive frequency bands. The source of the reflected radiance can be the sunlight or an active illumination source which is explicitly placed in the scene. While the active systems with illumination sources [8], [9], [10], [11], [12], [13], [14], [15], [16], [17], [18], [19], [20] might offer better detection performances, the passive systems [21], [22], [23], [24], [25], [26] using only sunlight provide a wider range of applications in practical scenarios. The captured radiance is converted to reflectance spectra, if the utilized region is a reflection dominant region, such as visible near-infrared (VNIR) and short-wave infrared (SWIR) bands. If the utilized region is the thermal dominant region including the middle-wave infrared (MWIR) and long-wave infrared (LWIR) spectrum, the radiance is then converted to emissivity spectra. The resulting reflectance/emissivity spectra for the pixels are visually inspected in comparison with the reference explosive spectrum for manual judgment [10], [11], [12], [13]. The similarity between the tested and reference spectra can be further evaluated with automatic signal detection methods based on target and background statistics [11].

TABLE I
OVERVIEW OF THE GROUND-BASED HYPERSPECTRAL IMAGING SYSTEMS PROPOSED FOR DETECTION OF EXPLOSIVES AND THEIR TRACES

Study	System type	Illumination source		Capturing device		Target substances	Detection algorithm	Perf. evaluation
		Type	Utilized spectral frequency/range	Type	Spectral range			
Fuchs et al. [11]	Active LWIR	QCL laser	7.35 μm, 7.58 μm	Broadband infrared cam.	4.2 –10.5 μm	TNT	Ratio of abs. and nonabs. bands	Visual inspection on score images
Bernacki et al. [13]	Active LWIR	QCL laser	9.06–10.16 μm	Broadband infrared cam.	7.5–13 μm	RDX	NDI, SFF, MF, MTMF	Visual inspection and comparison of pixel and reference spectra
Macarthur et al. [16]	Active LWIR	QCL laser	8 μm	Dual comb spectrometer	7.58 – 7.80 μm	RDX and PETN	Correlation coefficient (CC)	Comparison of pixel and reference spectra; visual inspection on correlation scores
Finton et al. [17]	Active LWIR	QCL laser	6.02 – 11.17 μm	Broadband infrared cam.	Not reported	AN, PN and tetryl	Not performed	Comparison of pixel and reference spectra
Breshike et al. [18]	Active LWIR	QCL laser	6 – 11 μm	Broadband infrared sensor	6 – 11 μm	RDX and PETN	Not performed	Comparison of pixel and reference spectra
Blake et al. [25]	Passive LWIR	Sunlight	Broadband	Hyperspectral LWIR cam.	7.7– 11.8 μm	HMX,TNT, RDX	PCA, MFA, MF	Visual inspection on score images
Ruxton et al. [21]	Active SWIR/ MWIR	OPO-based laser	1.5 –1.8 μm, 2.6 –3.7 μm	Broadband SWIR and MWIR cams	0.9– 2.1 μm, 2.5– 4 μm	Aspirin and hexamine	Not reported	Visual inspection and comparison of pixel and reference spectra
Onat et al. [24]	Passive SWIR	Sunlight	Broadband	Hyperspectral SWIR camera	1.5– 1.8 μm	PETN,TNT RDX, AN	Spectral-difference based metric	Investigation of metric values
El-Sharkawy et al.[19]	Active VNIR	Multispectral light source	(457, 488, and 514 nm)	Hyperspectral VNIR camera	400 – 1000 nm	RDX, HMX, and TNT	Not performed	Comparison of pixel and reference spectra; visual inspection on single band images
Abdallah et al. [28]	Passive VNIR	Broadband light	200 nm – 3.5 μm	Hyperspectral VNIR camera	375 – 1050 nm	TNT	Not performed	Visual inspection on single band images
Chaudhary et al. [20]	Active VNIR	Halogen lamb	Not mentioned	Hyperspectral VNIR camera	400 – 1000 nm	C4, AN, TNT	Support vector machines	Accuracy and kappa coefficient

Table I gives an overview of the present HSI studies for explosive detection. Although the table does not cover all the methods, it presents the main aspects of the proposed solutions in the existing literature, such as the type of the explosives, utilized source for the illumination, the spectral region of the proposed systems, the adopted algorithms for detection, and the main merits of performance evaluation. The present HSI studies for explosive detection have mainly targeted the detection of ammonium nitrate (AN), ammonium nitrate-fuel oil (ANFO), trinitrotoluene (TNT), hexahydro-trinitro-triazine (RDX), and their variants as they form the main components of improvised explosive devices. In addition, there are also studies for more sophisticated explosives, such as C4 [20].

The proposed systems utilize the emissivity characteristics of these explosives in LWIR range (6–11 μm) for detection [11], [13], [16], [17], [18] or the reflectance characteristics in the VNIR (0.6–1 μm) and SWIR (1.4–1.7 μm) range [19], [20], [21], [26]. The main illumination source for the active detection systems in LWIR spectrum [16], [17], [18] are selected as quantum cascade lasers to generate radiation at the desired wavelengths. More conventional sources, such as broadband illumination sources with their wider spectral characteristics, are also preferred in VNIR, SWIR, and MWIR systems [20], [21], [28]. The current status of all these studies is however still at the experimental validation stage in controlled or laboratory environments. Therefore, their usage for surveillance applications is not possible yet in the current state-of-the-art of this technology.

While surveillance systems with conventional red, green and blue (RGB) and thermal cameras have recently enabled extensive intelligent applications, such as automatic person identification [29], anomaly detection [30], face recognition [31], [32], and crowd analysis [33], HSI-based surveillance systems for dynamic scenes with moving vehicles and people imposes different requirements than the existing laboratory based HSI systems [1], [2]. First of all, the existing HSI studies for explosive detection are realized by using a limited number of test images in indoor or outdoor environments. An HSI surveillance system requires a more complete evaluation procedure covering the performances for different times and days depending on the orientation between the sun and the scene. Second, reported durations in current systems for the capturing of the scene are mostly dependent on the acquisition times of the snapshot HSI sensors, which are not sufficient for a real-time construction of spectral cubes for moving vehicles. Therefore, effective solutions should be developed to register the spectral bands captured at different instants of a moving object. Third, an HSI-based surveillance system requires white references in a scene for reflectance conversions different from the conventional CCTV surveillance cameras. While the usage of white references in temporary setups is feasible for the performance evaluations, an HSI surveillance system should have more sustainable and

secure solutions for the reflectance conversions with no requirement for white references in the targeted scene.

Another aspect of the current HSI studies for explosive detection is the lack of a full exploitation and analysis of the current state-of-the-art of hyperspectral detection algorithms. As indicated in Table I, the utilized algorithms for explosive detection are mostly limited to ratio based, correlation based, or matched-filter-based methods without providing detailed analysis for comparisons. The performances of main classes of methods in hyperspectral detection literature, such as orthogonal subspace methods and hybrid methods, were not completely addressed for explosive detection. In addition, learning- and deep-learning-based methods are another aspect to be explored for a ground-based HSI-based surveillance system designed for explosive detection.

Finally, the performance analysis of the current HSI systems for explosive detection is mostly performed by visually examining the similarities of the pixel spectra to the reference spectrum as well as the contrast at ground truth (GT) locations on the resulting score image after the detection. However, performance evaluation of these systems by using precision and recall (P-R) curves is not widely utilized, except for a few works on synthetically generated data. This situation can be explained by the low number of images for real case scenarios and the difficulties to form the GT masks as the solutions of explosive materials prepared for the experiments do not indicate a uniform distribution after they dry. As a final reason, most of the past research on this topic was mostly initiated by government and defense institutions, while the signal processing research community has later focused on the topic after HSI systems become more available in the market. Within the scope of the given state-of-the-art, the presented research on HSI surveillance system for explosive detection was triggered in 2017 after the successive bombing events with the car bombs in the capital of Turkey. After those events, HSI surveillance systems were adopted as a potential solution for standoff detection of such threats. In this regard, our aim in the related research was to develop a complete HSI surveillance system including the main parts such as setup, capture, reflectance conversion, and detection. The ultimate application for the proposed system is to be able to track the car bombs by locating the developed surveillance system on some specific points on high ways and at static control points in front of public buildings.

An HSI surveillance system for such an application on highways and control points should explicitly address the following challenges:

1) The reflectance conversions should be independent from the white references, as it is not possible to expose the position of the white references in a practical sustainable system.
2) The detection performances should be independent from time and date as much as possible. In contrary to the related literature using only a few test images in laboratory environment, the performances should be reported for a wider range of images covering real scenes in daily light.
3) The system should address the detection of different forms of explosives including granular or residual forms by designing necessary experimental setup with proper GT information, which is a challenging problem for residual explosives due to the difficulties to determine the exact pixels of the GT.
4) The main classes of target detection methods developed in the HSI literature should be properly adapted to the proposed surveillance system by deciding on the necessary selections and modifications regarding the method parameters, target signatures, and background information.

The first two parts of this article, which are previously published in a special issue of IEEE JSTARS in December 2019, were on the state-of-the-art [1] and reflectance conversions [2] for such a surveillance system. This article is therefore structured as a follow-up and final part of this complete surveillance system, which focuses on the detection of different forms of explosives and the design of related experiments. To the best of our knowledge as authors, the presented work is the first work on an HSI surveillance system for explosive detection, which holds the following conditions:

1) It proposes a complete technical framework from capture and reflectance conversion to the target detection.
2) It designs various experiments for different cases of explosives in real environment including granular and sprayed residues, fingerprint residues, and explosive traces on vehicles.
3) It develops an index-based method by utilizing the information of various spectral bands of the targeted explosive and reveals the most crucial spectral bands for detection.
4) It adapts and implements the signature-based and deep-learning-based methods to the given surveillance framework by using the spectral characteristics of the explosive materials and the fixed background scene.
5) It presents and compares their detection performances by means of the main merit of evaluation in target detection, namely, P-R curves, which is not performed in the previous literature.

The rest of the article is organized as follows. Section II describes the details of the proposed framework. The adaptation and implementation details of the main classes of target detection methods to the proposed surveillance framework for explosive detection are also presented in this section. Then, the designed experiments are presented in Section III, which is followed by the experimental results and comparisons in Section IV. The discussions are given in Section V. Finally, Section VI concludes this article.

II. Proposed Hyperspectral Imaging System and Target Detection Methods

Fig. 1 illustrates the main stages of the proposed HSI system for explosive detection [2]. The reflected light from the scene illuminated by the sunlight first passes through the liquid crystal tunable filter (LCTF). The spectral range between 900 and 1700 nm is scanned by the filter with a step size of 10 nm. The filtered light at each frequency is captured by a broadband SWIR sensor. The captured images at each frequency are then cascaded to form

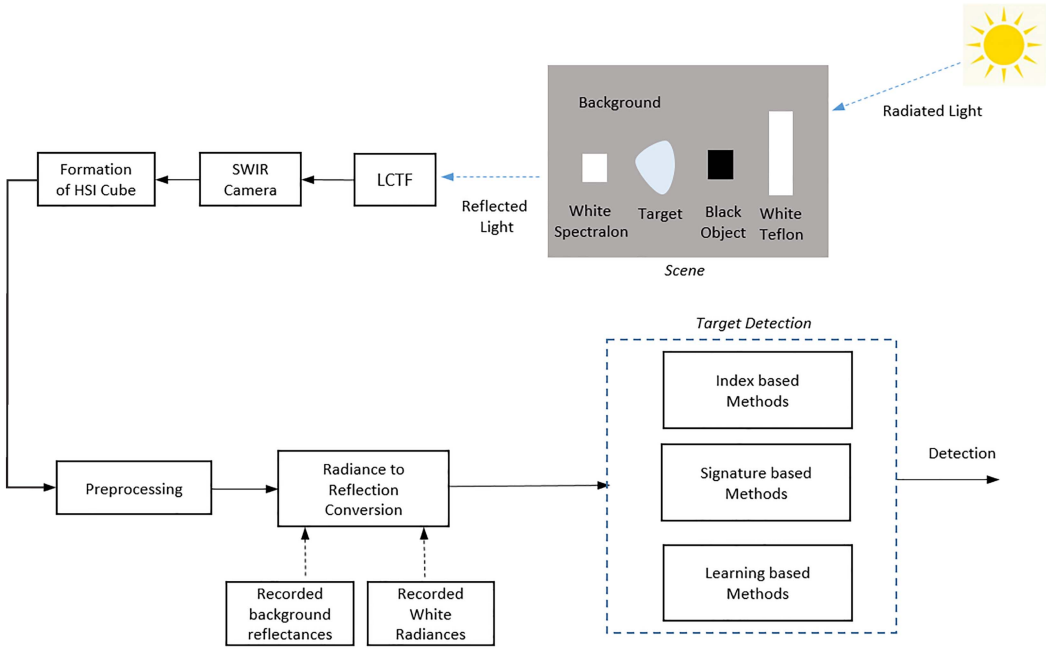

Fig. 1. General scheme of the proposed hyperspectral imaging system.

the spectral cube. This is followed by a preprocessing stage for noise removal.

The captured radiance is transformed to reflectance values. This conversion can be performed by using an incident radiance of a white Spectralon in the scene, by using the previously recorded radiances of the white Spectralon, or by using the recorded reflectance values of the background in a surveillance system with a fixed camera. All these options are discussed and compared in [2]. The present article performs the standard reflectance conversion by using the radiance of the white Spectralon and black reference to compare the performance of the proposed target detection method for the prepared experimental setups for different conditions. Given the radiance of a pixel, $R(\lambda)$, the reflection conversion is realized as

$$r\ (\lambda) = \frac{R\,(\lambda) - B\,(\lambda)}{W\,(\lambda) - B\,(\lambda)} \tag{1}$$

where $r(\lambda)$ is the resulting reflectance, and W and B are the spectral radiances of white and black references, respectively.

The detection is performed on the reflectance cube at the last stage. Inspired by state-of-the-art of hyperspectral target detection and classification methods, three approaches are adopted for explosive detection on HSIs in the SWIR range. First of all, in accordance with the widely utilized indexes in land cover classification and mineral identification, such as water, vegetation, and hydrocarbon indexes, the absorption bands of explosive chemicals are investigated for detection. Second, the widely utilized spectral signature-based methods ranging from covariance methods using background distribution to hybrid methods combining spectral matching with unmixing are adapted and analyzed for explosive detection. Finally, the current trend of deep-learning-based classification is explored for explosive detection in addition to the conventional methods, such as support vector machines (SVMs).

The details of each detection approach are presented in the following subsections by the following notation:

$$\begin{aligned} \boldsymbol{r} &= [r(\lambda_1)\ \mathrm{r}(\lambda_2) \ldots\ \mathrm{r}(\lambda_p)]^T \\ \boldsymbol{s} &= [s(\lambda_1)\ \ s(\lambda_2) \ldots\ s(\lambda_p)]^T \end{aligned} \tag{2}$$

where $\boldsymbol{r}$ and $\boldsymbol{s}$ denote the p-dimensional vectors corresponding to the spectrum of a pixel and the reference spectrum of the target, p is the number of spectral bands, and T is the transpose operation.

A. *Index-Based Methods*

Index-based methods use specific bands where the spectral characteristics of the target materials indicate significant changes for identification. Typical examples of such methods include normalized difference vegetation index [34], which is defined in terms of the near-infrared band and the visible red band, normalized difference water index [35], modification of normalized difference water index [36], normalized soil moisture index [37], and normalized soil difference [38]. Such indexes are generally used for land cover and land use mapping on the investigated regions.

Index-based methods are also considered in hyperspectral explosive detection literature. As typical examples, an index-based system operating in the LWIR range for detecting TNT traces on car paints and aluminum is proposed by Fuchs et al. [10]. The detection of TNT in the proposed model is achieved by taking the ratio of the broadband images obtained for the two tuned wavelengths of the laser source. One of these bands is chosen in the TNT absorption band at about 1360 cm^{-1} and the other outside this absorption band at about 1320 cm^{-1}. Another

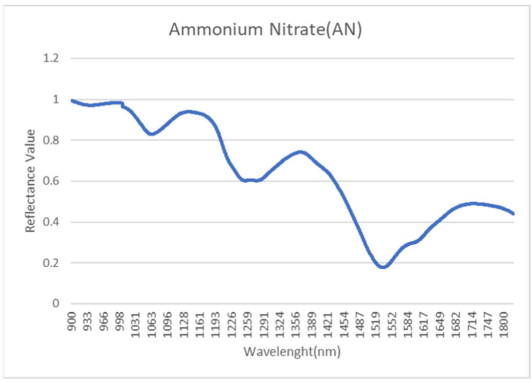

Fig. 2. Spectral signature of ammonium nitrate recorded with ASD spectrometer.

method is presented by Bernacki and Ho [12] for the detection of RDX and Tetryl in the LWIR range. The proposed system utilizes a pair of CO_2 lasers, which are set to the absorption and nonabsorption bands of RDX (∼9600 and ∼9250 nm). Similar indexes are also proposed for passive identification of explosives in the SWIR range [24].

Our proposed index-based method is based on the utilization of not only a single ratio, but more than one ratio of the specific bands of the target material. The method is tailored for the detection of AN as one of the frequently encountered explosives around the globe. The reflectance of AN is presented in Fig. 2. The selected bands for the ratios are λ_{b1}= 1030 nm, λ_{b2}= 1060 nm, λ_{b3}= 1280 nm, λ_{b4}= 1350 nm, and λ_{b5}= 1550 nm. These bands correspond to reflection or absorption bands where AN exhibit its characteristic chemical properties. The model works with the assumption that the ratios between different bands should be similar on different occasions.

The algorithm is based on whether the following ratios of the bands for each pixel of the HSI is within a predetermined interval of the ratios of the AN spectrum recorded with an ASD spectrometer:

$$\begin{aligned} \mathrm{th}_{1a} < \frac{r(\lambda_{\mathrm{b2}})}{r(\lambda_{\mathrm{b1}})} < \mathrm{th}_{1b},\ \mathrm{th}_{2a} < \frac{r(\lambda_{\mathrm{b2}})}{r(\lambda_{\mathrm{b3}})} < \mathrm{th}_{2b} \\ \mathrm{th}_{3a} < \frac{r(\lambda_{\mathrm{b4}})}{r(\lambda_{\mathrm{b3}})} < \mathrm{th}_{3b},\ \mathrm{th}_{4a} < \frac{r(\lambda_{\mathrm{b4}})}{r(\lambda_{\mathrm{b5}})} < \mathrm{th}_{4b}. \end{aligned} \tag{3}$$

Given the HSI, the algorithm first computes the ratios given in (3) for each pixel. The ratio image for each of the given four cases is binarized by simply assigning one to the pixels whose ratios are between the given thresholds, and assigning zero to the other pixels. For each threshold combination given in (3), the final image is obtained by applying AND operator to all resulting binary images. In order to generate the P-R curve for the given algorithm, the thresholds $(\mathrm{th}_{1a}, \mathrm{th}_{1b}, \mathrm{th}_{2a}, \mathrm{th}_{2b}, \mathrm{th}_{3a}, \mathrm{th}_{3b}, \mathrm{th}_{4a}, \mathrm{th}_{4b})$ are swept between a minimum and maximum interval in the neighborhood of the GT ratios calculated from the AN spectrum.

B. Signature-Based Methods

Rather than the ratios of specific bands as in index-based methods, signature-based target detection methods use the advantage of the whole spectrum for detection. Until now, the signature-based methods have not been extensively utilized for the practical application of explosive detection in the outside environments. This article, therefore, focuses on the potential of different classes of signature-based detection methods for the purpose of explosive detection in ground-based surveillance systems.

Signature-based target detection methods can be classified into four classes [39], [40]. The similarity of the vectors is investigated in the first class of methods, which involves cross-correlation, normalized cross-correlation, and spectral angle mapper (SAM) [40]. Matched filter [41], adaptive coherence estimator (ACE) [42], and constrained energy minimization [43] can be categorized in the second class, which applies the correlation operation by suppressing the outputs for the background. The main difference between these methods is the different usage of mean and covariance matrices for the background modeling. The orthogonal subspace, which eliminates the effects of the endmembers forming the background during the matching operation, is used in the third-class methods [39], [44]. As a final class, hybrid methods [45] combine the outputs of the unmixing algorithms with the results of the correlation-based detection methods. In order to utilize these methods during the experiments, one representative is selected for each class, namely SAM, ACE, orthogonal subspace detector (OSP), and hybrid structured detector (HSD), for the mentioned four class, respectively. The selected algorithms can be briefly described as follows.

Let $\boldsymbol{r}$ and $\boldsymbol{s}$ denote the p-dimensional vectors corresponding to the spectrum of a pixel and the reference spectrum of the target as defined in (2). The angle between two spectral vectors is obtained as

$$\theta = \arccos\left(\frac{\boldsymbol{r}^T\boldsymbol{s}}{|\boldsymbol{r}|\,|\boldsymbol{s}|}\right) \tag{4}$$

which gives the SAM metric [28]. The similarity between the two vectors is high when the angle is small in (4). SAM metric ensures a more robust evaluation due to its invariance to scaling compared to the mean square error metric. On the other hand, the background information is not utilized during the detection as one of its lacks.

The background information is exploited in the ACE algorithm [29] while assigning a score to each pixel

$$T_{\mathrm{ACE}}(\boldsymbol{r}) = \frac{(\boldsymbol{s}^T\boldsymbol{C}^{-1}\boldsymbol{r})}{(\boldsymbol{s}^T\boldsymbol{C}^{-1}\boldsymbol{s})\,(\boldsymbol{r}^T\boldsymbol{C}^{-1}\boldsymbol{r})} \tag{5}$$

where $\boldsymbol{C}$ represents the covariance matrix of the background. Such a formulation suppresses the effect of the background pixels while maximizing the output for the target $\boldsymbol{s}$.

The suppression of the background is also achieved in the OSP detector [39] by transforming the spectra of the pixels to an orthogonal subspace of the background components. If the matrix containing the background spectral signatures is denoted

as $\boldsymbol{b}$, then the projection matrix, $P_b^{\perp}$, which is used to map the spectral pixels to the orthogonal subspace, is defined as

$$\boldsymbol{P}_{\boldsymbol{b}}^{\perp} = \boldsymbol{I} - \boldsymbol{b}(\boldsymbol{b}^{\boldsymbol{T}}\boldsymbol{b})^{-1}\boldsymbol{b}^{\boldsymbol{T}}. \tag{6}$$

To obtain the OSP score for each pixel, this projection matrix is applied to the spectrum of each pixel, as

$$T_{\text{OSP}}\ (\boldsymbol{r}) = \frac{\boldsymbol{s}^T\boldsymbol{P}_{\boldsymbol{b}}^{\perp}\boldsymbol{r}}{\boldsymbol{s}^T\boldsymbol{P}_{\boldsymbol{b}}^{\perp}\boldsymbol{s}}\ . \tag{7}$$

As it can be seen from (6) and (7), if $\boldsymbol{r}$ is one of the background components, then the result of the OSP would converge to zero.

For the HSD algorithm [45], the analysis of the scene is performed both physically and statistically by combining the unmixing with the signature-based methods to achieve a more robust detection performance. The unmixing method and detection algorithm are selected as fully constrained least squares [46] and adaptive matched subspace detector [45] in this method, respectively. The HSD method can be formulated as

$$T_{\text{HSD}}\ (\boldsymbol{r}) = \frac{(\mathbf{r} - \widehat{\boldsymbol{\alpha}_{\boldsymbol{b}}}\boldsymbol{b})^T\Sigma^{-1}\,(\mathbf{r} - \widehat{\boldsymbol{\alpha}_{\boldsymbol{b}}}\boldsymbol{b})}{(\mathbf{r} - \hat{\boldsymbol{\alpha}}\boldsymbol{e})^T\Sigma^{-1}\,(\mathbf{r} - \hat{\boldsymbol{\alpha}}\boldsymbol{e})} \tag{8}$$

where $\boldsymbol{e}$ matrix contains the background and target signatures, $\hat{\boldsymbol{\alpha}}$ is the vector containing the abundances of all endmembers, and $\widehat{\boldsymbol{\alpha}_{\boldsymbol{b}}}$ is the abundance vector of background signatures. The subtraction of the background components from the test pixels after modulation with the found abundances using unmixing is the main idea of the HSD method.

In the implementation of the abovementioned algorithms, the reference spectrum of the target, $\boldsymbol{s}$, is measured with the ASD spectrometer before the experimental setup is constructed. After the capturing and reflectance conversion of the HSIs, the covariance matrix, $\boldsymbol{C}$, is computed over all the pixel spectra of the HSI. The background matrix, $\boldsymbol{b}$, is formed by selecting a number of representative pixel spectra from the background of the captured scene. Depending on the scene and located position of the surveillance camera, these could be asphalt, concrete, soil, metal board, and other typical components.

C. Learning-Based Methods

The third group of methods investigated in this article is the learning-based methods for the purpose of explosive detection. While the signature-based methods use the spectral signatures of the target materials captured by a spectrometer, learning-based methods aim to detect the target materials by learning a model from the previously captured controlled data in the same scene. To this end, the performances of both conventional and state-of-the-art methods are investigated.

Support vector machine (SVM) is selected as the well-known conventional machine-learning method since it has better performance with its learning capability by using a small number of samples compared to the other statistical classification methods. SVM has been applied to different HSI analysis tasks, such as land cover classification [47], target detection [48], unmixing [49], and physical parameter estimation, such as temperature [50] and emissivity [51]. In this article, SVM is utilized for explosive detection as a two-class classification method.

The second method is selected from the state-of-the-art deep-learning-based methods. This recent trend of HSI classification uses hyperspectral pixels individually or as a patch, which corresponds to 3-D cubes. The performance of this latter approach, which is generally treated under the convolution neural network (CNN) structure, has been proved to be more successful than the algorithms using only pixel spectra [52], [53], [54]. As an example, Li et al. [52] proposed to use a CNN-based classification method obtained by a fully connected layer behind two 3-D convolution layers. Similar to these methods, Lee and Kwon [53] and Hamida et al. [54] also utilize CNN-based models for hyperspectral classification.

Different from these studies on the application of CNNs and graph convolutional networks (GCNs) for HSI classification, there are also studies which investigate fusion strategies between CNNs and GCNs to address the limitations of single models in HS image classification [55]. Another study, referred as general multimodal deep-learning (MDL) framework [56], aims pixel-level classification by combining pixel-based and spatial–spectral classification. Various modules are examined for fusion within the proposed MDL–RS Framework [56].

Finally, a target-detection-based method, UIU-Net, which is a novel framework for detecting small objects in infrared images, is introduced by Wu et al. [57]. UIU-Net incorporates a small U-Net into a larger U-Net backbone, allowing for multilevel and multiscale representation learning. The proposed method established promising results in small object detection, demonstrating its effectiveness and generalization capabilities.

By considering both speed and performance comparisons in the experiments, the Hamida model [54] is chosen to be employed in the proposed HSI surveillance system for explosive detection. Without loss of generality, the other networks can also be adapted to the given framework after necessary modifications. The training and testing of the utilized methods are performed by considering the main characteristics of a surveillance system such that the camera is fixed and records the same scene at different times. More particularly, an experimental setup involving a target explosive is constructed for capturing. The scene is then captured at different days from the same position. The data captured on one day are used for training and the data on the other day for testing. In order to form the labeled data for the target class, the GT positions of the granular explosives are determined delicately by using a higher resolution RGB camera. The labeled data for the background class is randomly selected from different positions.

Radial basis function (RBF) kernel is utilized in the implementation of SVM. In order to adapt the Hamida deep-learning model [54] to the given framework, a $3 \times 3 \times N$ cube is generated for each hyperspectral pixel by using its spatial 3×3 neighborhood. The label information of the middle pixel is preserved for the generated cubes used for training. Then, the training is performed with a deep-learning model formed of four 3-D convolution layers, two pooling layers, and one fully connected layer. The parameters of the model for each layer are given in Table II. The number of parameters in the given

TABLE II
PARAMETERS OF THE UTILIZED DEEP-LEARNING MODEL

	Feature size / Output size	Kernel	Stride	Padding
3-D conv layer 1	20	(3, 3, 3)	(1, 1, 1)	1
Pooling layer 1	20	(3, 1, 1)	(2, 1, 1)	(1, 0, 0)
3-D conv layer 2	35	(3, 3, 3)	(1, 1, 1)	(1, 0, 0)
Pooling layer 2	35	(3, 1, 1)	(2, 1, 1)	(1, 0, 0)
3-D conv layer 3	35	(3, 1, 1)	(1, 1, 1)	(1, 0, 0)
3-D conv layer 4	35	(2, 1, 1)	(2, 1, 1)	(1, 0, 0)
Flatten layer	–			
Fully con. layer	2	–	–	–

network varies according to the number of spectral bands in the hyperspectral cube. In this relatively small network structure, an 81-band hyperspectral cube has 68 962 parameters. Considering that the 3×3 neighborhood of each pixel is taken into account, the total number of computations increases depending on the number of pixels. The optimization algorithm in the implementation is selected as Adam's optimizer. The parameters of the training process are decided as 256 for the batch size, 0.001 for the learning rate, and 0 for weight decay. The process is performed over 10.000 epochs and no learning scheduler was used. The trained model is then tested with the hyperspectral data captured on a different day.

III. EXPERIMENTAL SETUP

Four different experiments are constructed for the performance evaluation of the proposed explosive detection methods for varying conditions including granular explosives, sprayed explosive residues, fingerprints, and real case scenarios for vehicles.

A. Experiments With Granular Explosives

The experimental setup for the performance evaluation on granular explosives is illustrated in Fig. 3(a) [2]. A broadband SWIR sensor (900–1700 nm) is utilized for the acquisition, which is cascaded with a VariSpec LCTF. The hyperspectral cubes are formed as described in Section II. The size of the hyperspectral cubes is $322 \times 640 \times 81$, where the dimensions refer to the width, height, and number of spectral bands, respectively. The spectral step size is 10 nm during capturing. Solid AN samples are used in the scene as the target explosives. The number of AN pixels in the GT position is about 1900. The same number of background pixels are utilized during the training of utilized deep-learning model for a balanced training between two classes.

The scene also includes a white Teflon, a standard Spectralon of 90° orientation with respect to the horizontal axis of the camera, another Spectralon with an orientation of 45°, and black object, which are utilized for reflectance conversion. Among different methods for reflection conversions [2], the conventional

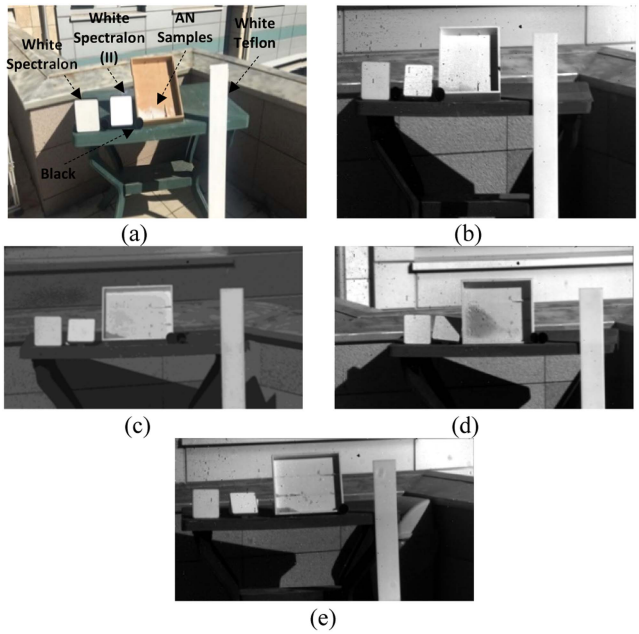

Fig. 3. (a) Experimental setup for solid explosives, and sample broadband SWIR images captured on (b) 13th October, (c) 18th October, (d) 3rd November, and (e) 16th November [2].

TABLE III
TIMES AND DATES OF THE IMAGE ACQUISITIONS AND WEATHER CONDITIONS [2]

Dates	Times						Weather max temp.
13th Oct	10:30	11:30	12:30	13:30	14:30	15:30	Clear/ slightly cloudy 20°C
18th Oct	10:30	11:30	12:30	13:30	14:30	15:30	Clear/ slightly cloudy 23°C
3rd Nov	10:30	11:30	12:30	13:30	14:30	–	Clear/ slightly cloudy 14°C
16th Nov	10:30	11:30	12:30	13:30	14:30	–	Clear/ slightly cloudy 18°C

one which uses the white Spectralon and black object in the incident scene is adopted in the experiments as described in (1). The acquisition of the HSIs is performed at different times and dates in a period of about one month as illustrated in Table III [2]. The acquisition was begun at about 10:30 and continued at every hour until 15:30. The camera distance was about 8 m. The weather was clear or slightly cloudy.

B. Experiments for Sprayed Explosive Residues

The next experiment is designed to investigate detection performances for sprayed explosive residues on the metallic body of a vehicle. Different aspects, such as the performances of different algorithms for sprayed explosives and the effect of the color paint and density, are considered for the investigation. Therefore, the metal plates are painted with five different car paints. The liquid AN solution, which is simply prepared as mixing solid AN with alcohol at a rate of 250 g/L, is sprayed homogeneously onto the colored metal plates in different amounts. Then, the performances are evaluated after the solution residues dry.

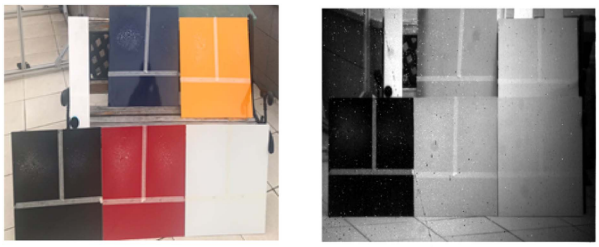

(a) (b)

Fig. 4. (a) Experimental setup for sprayed explosive residues which are densely sprayed (upper left side), sparsely sprayed (upper right side), and nonsprayed regions (bottom side), and (b) sample broadband SWIR image.

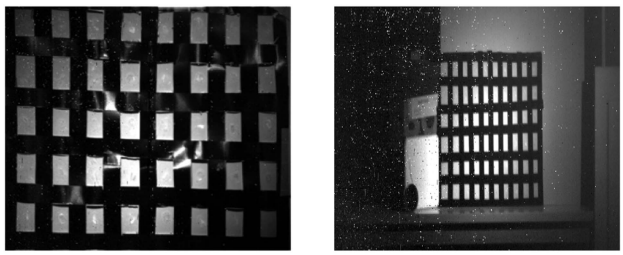

(a) (b)

Fig. 5. (a) Designed template to determine the location of fingerprint residues on the metal plate as ground truth. (b) Sample broadband SWIR image of the prepared setup for fingerprint experiment.

Fig. 4 illustrates the setup for the experiments. Three regions on each metal plate, namely, dense sprayed (upper left side), the sparse sprayed (upper right side), and nonsprayed regions (bottom side), are utilized for the comparisons. One important challenge during the experiments for the sprayed explosive residues is to determine the GT locations as the chemicals are accumulated nonuniformly after they dry. Therefore, the detection performances are inspected visually instead of P-R curves. This challenge for the quantitative performance evaluation of explosive residues is handled by designing a more rigorous experiment in the next section for fingerprint residues.

C. *Experiments With Fingerprint Residues on Metal Surfaces*

The scope of the proposed experiment covers the detection of fingerprint residues since fingers contacted with explosive materials can leave traces on the transported vehicles. The usage of P-R curves is challenging to evaluate the detection performances for fingerprints as it is difficult to determine the exact pixels in the GT. Therefore, a suitable setup as a 2-D array of fingerprints on a metal surface is prepared and a methodology for proper measurement of detection rates and false-positive rates is developed over the number of found fingerprints and the total number of fingerprints.

The experimental setup for the fingerprints on metal plates is illustrated in Fig. 5(a) and (b). First, a template which constitutes 50 rectangles is prepared using black tape. The template is attached to the white metal plate in order to determine the exact location of the fingerprints. The fingers that are exposed to the AN solution are then contacted to the metal plate inside every rectangle. After they dry, the resulting fingerprints inside each rectangle are used together instead of individual pixels to determine detection performance.

For this purpose, the approximate size of the fingerprints is determined. The number of detected pixels at a threshold value is counted inside a sliding window, whose size is determined according to the approximate size of the fingerprints. If the rate of the detected pixels is greater than the predetermined value, then it is accepted that the target is present. If the detected areas are inside the rectangles (Fig. 5), then they are assumed as true positives. If not, they are assumed as false positives. The P-R or receiver operating characteristics curves can then be obtained by applying these operations for each threshold value.

(a) (b)

Fig. 6. Experimental setups for sprayed explosive residues with (a) distance (∼7 m) and (b) distance (∼15 m).

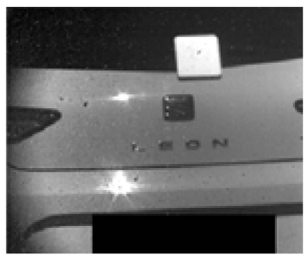

Fig. 7. Experimental setups for two different solid explosives (AN, RDX) on the same scene. The distance to the vehicle is about 7 m.

D. *Real Case Scenarios on Vehicles*

The detection of explosive residuals on vehicles was one of the main targets of the performed research. Therefore, some example setups from those tests are also presented here. The first case, which is illustrated in Fig. 6(a) and (b), is designed by touching the hands with the AN solution and then pressing hands onto the car's trunk. The performances of different algorithms for two different distances are evaluated. As the second case, the solid AN and RDX are applied onto the car's trunk as shown in Fig. 7. The capability of different algorithms for a scene composed of different explosives is investigated.

IV. Experimental Results and Comparisons

The performances of the index-based, signature-based, and learning-based target detection methods are compared for the designed experiments both visually and in terms of P-R curves.

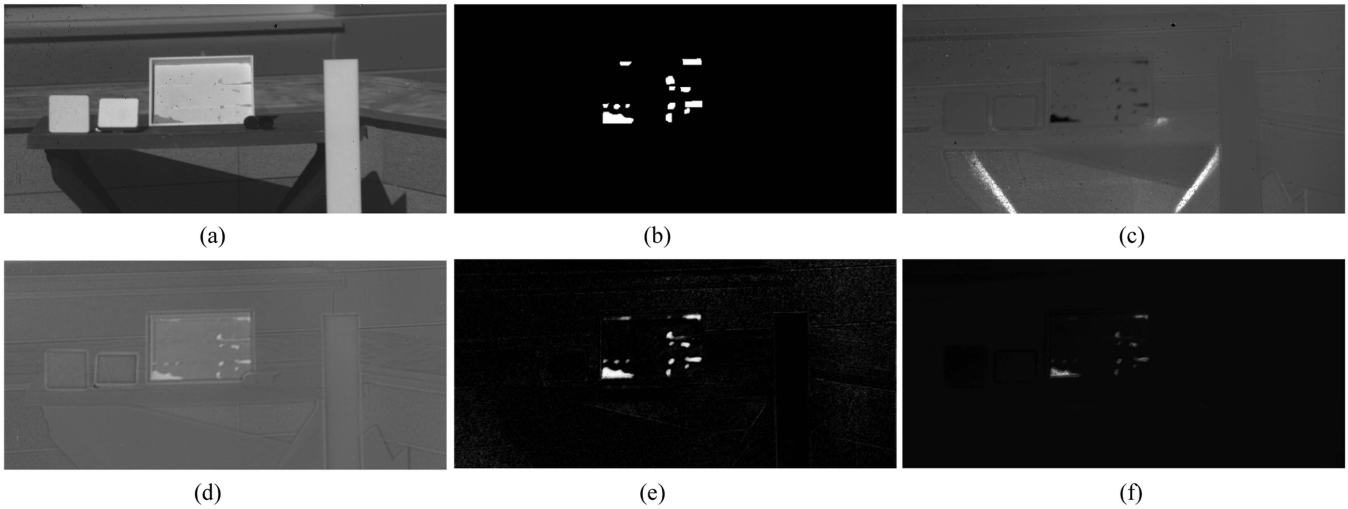

Fig. 8. (a) Sample broadband SWIR image, (b) ground truth image for the experiment of solid explosives, (c), (d), (e), and (f) score images obtained for SAM, OSP, ACE, and HSD algorithms, respectively.

In order to obtain the P-R curves, the score image for a detection algorithm is thresholded and the pixels greater than the threshold are labeled as target pixels. The precision is computed by dividing the number of correctly found pixels by the total number of labeled pixels. The recall is computed as the ratio of the correctly found pixels to the total number of pixels in the GT. The ultimate P-R curve is obtained by calculating the P-R values by changing the threshold value between the minimum and maximum in the score image.

Without loss of generality, the adopted strategy, namely P-R curves over pixels, is the baseline and standard performance evaluation to assess the performance of the methods and overall system. This is applied to all the detection methods for a fair comparison. After the detection over pixel levels, the false-positive rates can be decreased with the decision over more pixels depending on the targeted application. These selections are dependent on the targeted application and the risk of missed detection and cost of false detection. The next subsections present the results for each of the designed experiments.

A. *Experiments and Comparisons for Solid Explosives*

The algorithm comparisons are first presented in this section beginning with the signature-based methods. Fig. 8 shows the GT and the results of the signature-based target detection algorithms for the dataset prepared for the detection of solid explosives. The target detection performances for the four representatives of different signature-based detection algorithms (Section II-B), which are selected as SAM, OSP, ACE, and HSD, are presented in the figure. It should be noted that the scores for the algorithms OSP, ACE, and HSD are directly proportional with the similarity between the pixel spectrum and target spectrum while it is inversely proportional in the case of SAM. The SAM algorithm separates the target pixels from other materials as illustrated in Fig. 8(c) with black regions. However, there are also some false alarms in the background. The score map of the

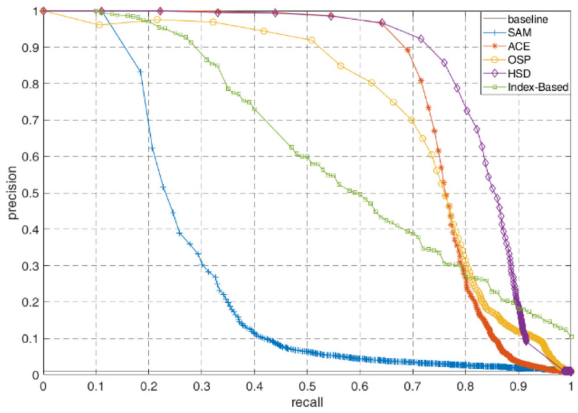

Fig. 9. Precision–recall curves for different algorithms. Average precision values are 0.825, 0.757, 0.712, 0.598, and 0.268 for HSD, ACE, OSP, index-based, and SAM, respectively.

OSP algorithm shows that the background is suppressed and the false alarms are lower than the ones in the case of SAM. The false positives are also apparent in some background regions on the score map of the ACE algorithm. On the other hand, the HSD algorithm performs the background suppression better than the other algorithms due to the combination of unmixing and the signature-based target detection algorithms.

In order to evaluate the quantitative performances of these algorithms, P-R curves which are obtained by using the GT image are presented in Fig. 9. The best performance while interpreting P-R curves is accepted as the closest point to the right-top side of the curve, which gives the high precision and high recall values. The average precision over all recall values is regarded as another indicator of the detection performance. In this context, we have observed that the HSD algorithm gives the best performance in terms of both indicators. The HSD algorithm is followed by the ACE algorithm especially with the lower precision values at higher recall values. Another observation is the degradation

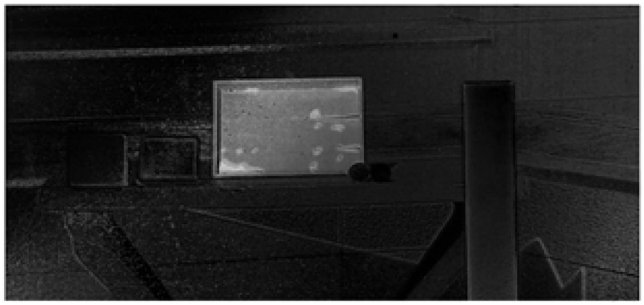

Fig. 10. Resulting score image for index-based method.

TABLE IV
SPECIFIC PRECISION AND RECALL VALUES FOR DIFFERENT ALGORITHMS

	Precision	Recall
SVM	0.97	0.10
Hamida	0.98	0.11
Fully connected	0.84	0.17
Index-based (precision> 0.9)	0.90	0.23
Index-based (recall> 0.9)	0.13	0.90
HSD (precision> 0.9)	0.92	0.72
HSD (recall> 0.9)	0.14	0.91

in the performance of the SAM algorithm due to the lack of background modeling producing a high number of false alarms in the background. The remaining tests are presented for only the HSD and ACE algorithms due to their better performances.

Another aspect of the experiments is the performance of index-based methods given in Section II-A. Index-based methods aim to determine the target using the ratios in different bands. The band ratios obtained from the spectral signature captured with the ASD spectrometer are used as the GT ratios in order to form the P-R curve in Fig. 9. Compared to the other signature-based and learning-based methods, the performance of index-based method is lower, in particular, for the cases where high precision is required. However, the proposed index-based method is still quite efficient when recall values higher than 90% are required.

Fig. 10 shows the final image which is obtained by the multiplication of the pixels that satisfy four different ratio information given in Section II-A. The AN regions are quite prominent in the final image. When the ratio information is examined separately in our visual analysis, it is observed that the fourth ratio in the index-based method has a higher effect than the others. In regard to the utilized bands for the fourth ratio in (4), the spectral range of (1350–1550 nm) is the most distinctive region of AN with respect to the background. The detection performance for each ratio information is quite low. However, when ratio information is fused together, their performance is getting higher.

Table IV presents the P-R values returned by the (deep) learning-based algorithms. In order to have a consistent comparison with learning-based algorithms which detect targets with high precision values, the results for the index and signature-based methods are also presented in Table IV for the case where precision values are higher than 90%.

Although it is generally desired to reach high P-R values in target detection algorithms, it might also be necessary to make a choice between P-R values. For instance, if the target is highly risky as in the case of bombings, it is desirable to have a quite high recall value or inversely, a very low missed detection rate. Therefore, the performances where the recall values are higher than 90% are also included in Table IV. The final images obtained with the algorithms for the given P-R values in Table IV are shown in Fig. 11. While presenting the resulting binary images, the threshold is selected as the value, which gives the closest precision value to 0.9 in Fig. 9.

As can be revealed from the table, the recall values of learning-based methods (SVM, Hamida, fully connected network) are quite low. However, the ultimate precision values are in the range of 84%–98%. While the fully connected network achieves 84% of the precision rate, the recall value is as low as 17%. On the other hand, Hamida and SVM methods give similar P-R performances. When these learning-based methods are compared with the HSD algorithm, the HSD algorithm obtains much higher recall values in similar precision values. HSD algorithm first applies unmixing to the data to eliminate the background components. These background components are subtracted from the hyperspectral pixels with respect to their abundances. Therefore, the separation of background components from hyperspectral pixels provides a better correlation with the GT target signature.

B. *Experimental Results for Sprayed Explosive Residues*

The results of the experiment designed for the sprayed explosive residues are shown in Fig. 12. As it is not possible to precisely determine the GT pixels after they dry, the results are only evaluated visually. It can be inferred from the results that the algorithms are compatible with the results of solid explosives. Although the ACE algorithm returns the higher values for the target pixels, there are a lot of noisy pixels from the background. HSD algorithm suppresses the background noise more successfully. In particular, it indicates noticeable results to detect the mixed pixels which consist of metal plates and sprayed explosive residues. The dense sprayed parts are detected better in all algorithms than the sparse sprayed parts, as expected.

C. *Experimental Results for Fingerprints*

The experimental results for fingerprints are crucial to evaluate the detection performances for the proposed system.

The main effort in these experiments is to overcome the problem of creating GT data. Although we have designed a regional pattern to bound the GT, the fingerprints do not fill the regions. Therefore, we have decided to apply postprocessing as explained in Section III-C. In more detail, if the number of positive pixels in a sliding window is greater than 20% of the 8×8 area, then the target is assumed as present. The true positive, recall, and false-positive values are computed by using the GT information by repeating this windowing operation for each threshold level. The false-positive rates, when the recall value is maximum, are given in Table V. Fig. 13 gives also the visual results for the detected fingerprints along with the GT. Accordingly, HSD and ACE algorithms reveal high detection

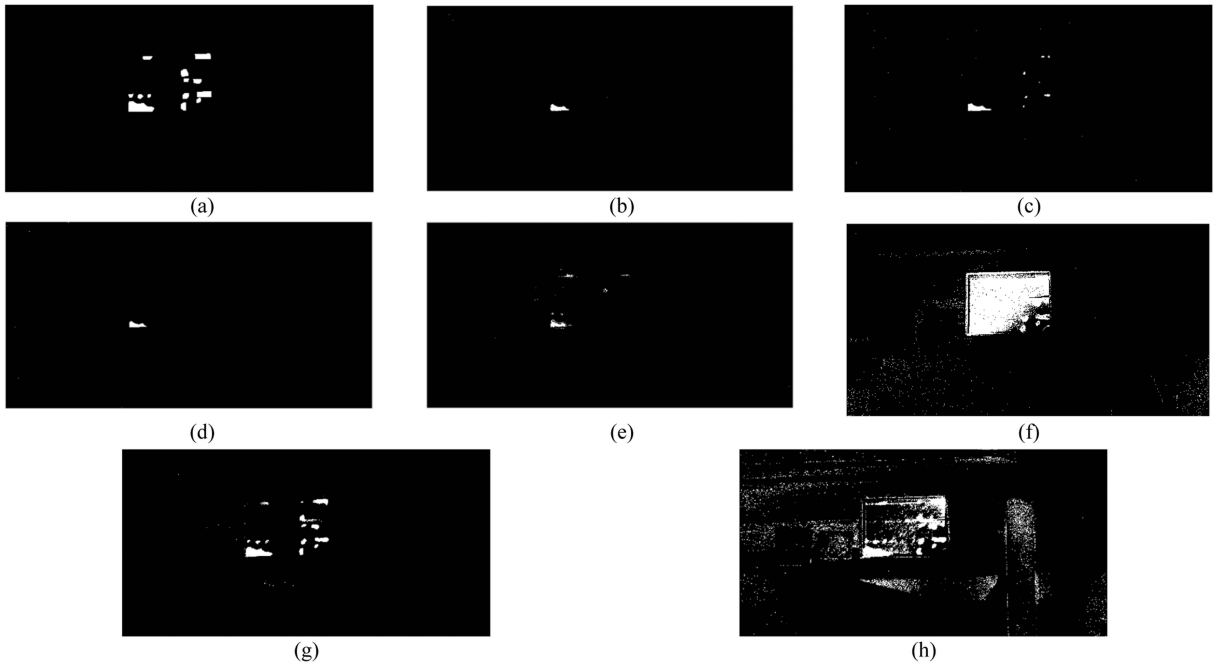

Fig. 11. (a) Ground truth and detection results for (b) Hamida, (c) fully connected neural network, (d) SVM, (e–f) index-based method (precision $>$ 0.9 and recall $>$ 0.9, respectively), and (g–h) HSD (precision $>$ 0.9 and recall $>$ 0.9, respectively).

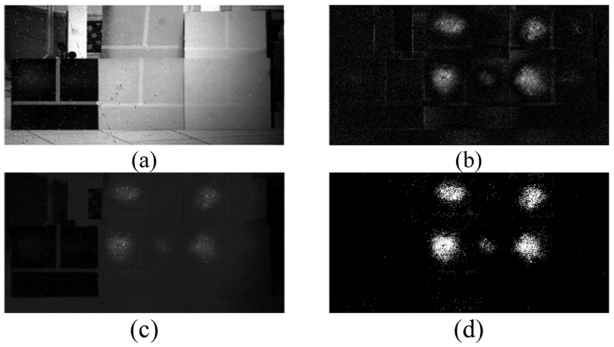

Fig. 12. (a) Sample broadband SWIR image for the experiment of sprayed explosive residues, (b) and (c) score images obtained for ACE, and HSD algorithms, respectively, and (d) thresholded HSD score image.

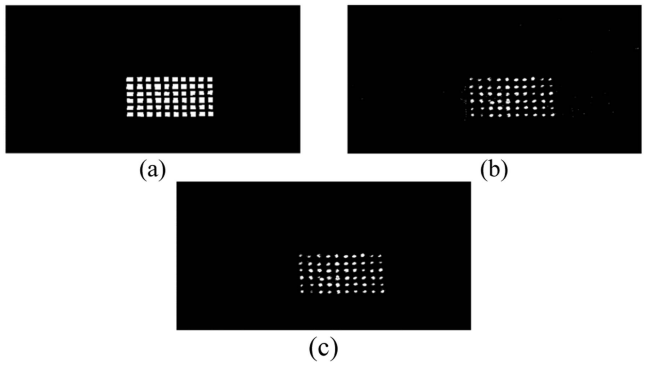

Fig. 13. (a) Ground truth image, (b) HSD score image, and (c) postprocessed HSD score image.

TABLE V
FALSE-POSITIVE RATE WHEN THE RECALL VALUE IS 100% FOR ACE AND HSD FOR FINGERPRINT EXPERIMENT

Algorithm	False positive rate (%)	Recall (%)
ACE	0.02	100
HSD	0.005	100

performances with low false-positive rates, as expected due to their successful background modeling.

As another aspect of the experiments, we investigate the effect of the number of the used bands on the target detection performance in Fig. 14. The numbers of the utilized bands are

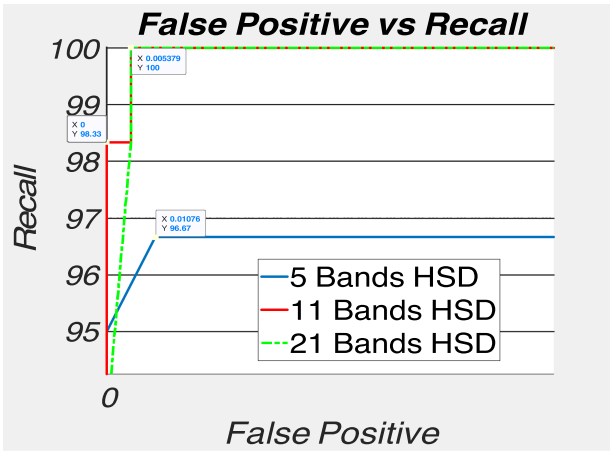

Fig. 14. False positive-recall graph for different number of bands.

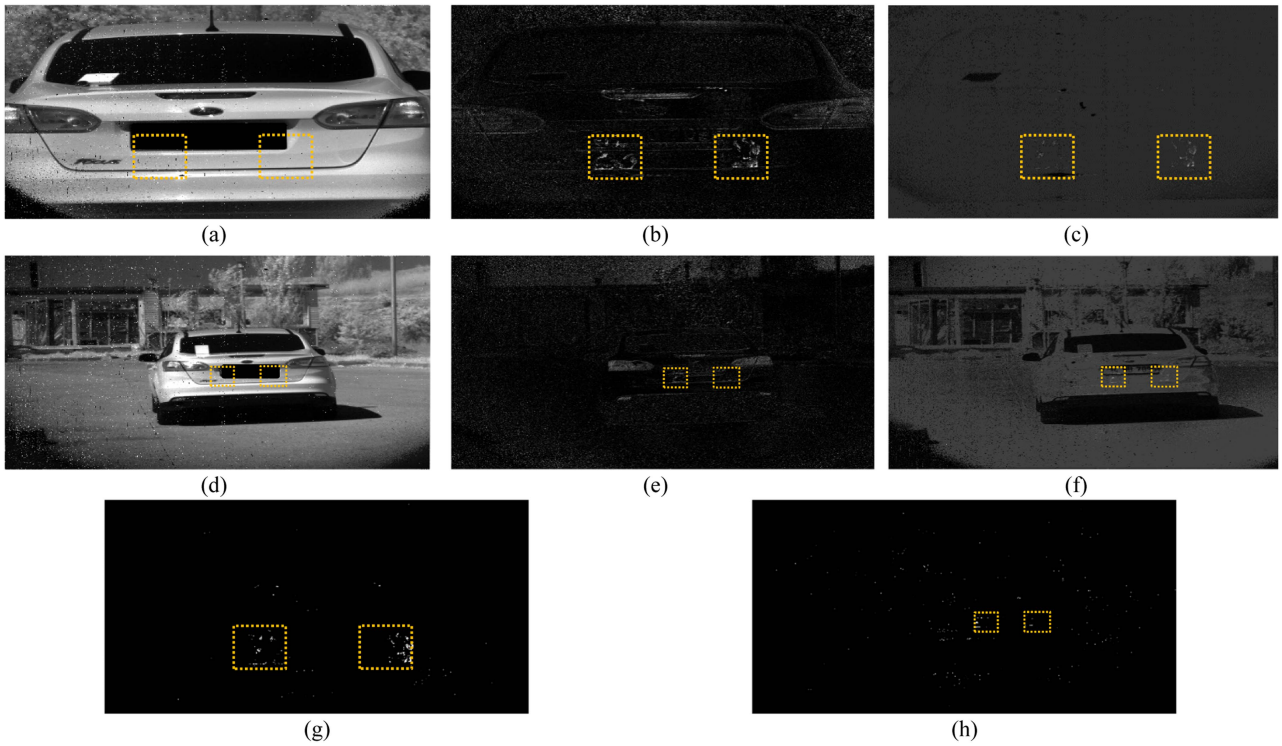

Fig. 15. (a), (d) Sample broadband SWIR images for the captured hyperspectral image of the vehicle with explosive residues on its trunk from about 7 and 15 m, respectively, (b) and (e) score images obtained for the ACE algorithm, (c) and (f) score images obtained for HSD algorithm, and (g) and (h) thresholded HSD score images for both scenes, respectively. The dashed regions indicate the positions where the hands with the ammonium nitrate solution are touched.

selected as 5 and 11 in the same wavelength interval, in addition to the original number of bands, which is 21 in the previous tests. The experiment reveals that 11 bands give comparable results to the case of 21 bands by reaching the maximum recall value with the same false-positive rate, which is at a very low level around 0.005%. On the other hand, when five bands are used, the detection performance drastically decreases. According to these results, at least 11 bands are necessary to achieve sufficient detection performances.

D. Experimental Results for Real Case Scenarios

The last experiments in the performed research are to investigate the performance of the proposed algorithms in two different real case scenarios. Fig. 15 shows the detection results for ACE and HSD for the case when hands with the sprayed explosive residues are pressed on the trunk of the car. Compared to the ACE, the HSD algorithm is quite successful in detecting residuals on the trunk of the car. However, there are some false positives as individual pixels in the results. As also indicated in the results for different distances, the false-positive rate decreases when the car is getting closer to the hyperspectral sensor.

Fig. 16 shows the detection results for the other case where solid explosive residuals are pasted on the car trunk. AN and RDX are selected as explosives for this experiment. Both of the algorithms detect the AN and RDX residuals successfully as indicated in the figure.

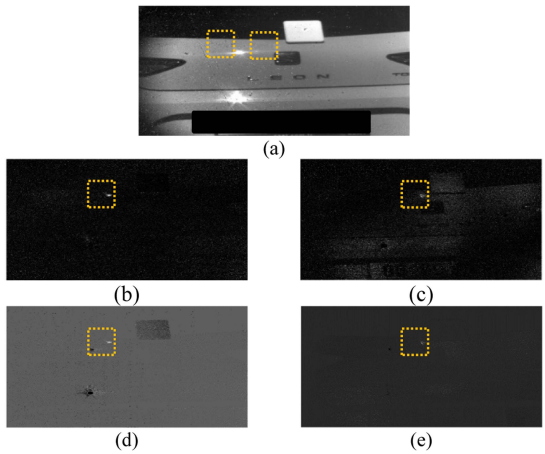

Fig. 16. (a) Sample broadband SWIR images for the experiment of real case scenario, (b) and (c) ACE score images obtained for AN and RDX, respectively, and (d) and (e) HSD score images obtained for AN and RDX, respectively. The dashed regions indicate the positions of AN and RDX in the figures.

V. Discussions

We have investigated different aspects of the proposed HSI surveillance system in the discussions. As there is not end-to-end HSI surveillance system proposed for explosive detection until now, we have encountered various challenges to be addressed from the beginning to the end of the performed research. One of the first concerns for the success of the system was to design the correct experimental setups for the

detection of explosives, which can be found in bulk, granular, or residual forms depending on the targeted application. For this purpose, we prepared four different experimental setups for the detection of granular explosives, residual explosives, fingerprints residues on metal surfaces, and residues on vehicles.

While the previous literature on explosive detection mainly concentrates on laboratory solutions, they were mostly analyzing the detection performances by visually checking the score images and/or comparing the pixel spectra at GTs with the spectral signatures of the targeted explosives. However, our main aim in this article was to adapt and compare the detection performances of the three main class of hyperspectral target detection methods for explosive detection and to reveal the best one in the context of a surveillance system. Therefore, we have preferred to realize the performance evaluation by means of P-R curves as the standard evaluation in signal detection.

While comparing the performance comparison of three main classes of methods, a successive approach was adopted to arrive concise conclusions without losing the main focus among many possibilities. To this end, we have first revealed the choices for the selected bands in index-based methods. Then, the performances of index-based methods and the main signature based methods, namely SAM, ACE, OSP, and HSD, are compared in terms of P-R-curves. After revealing that HSD is the best method among signature-based methods, the comparison is further performed with the learning-based methods over specific P-R values in the last analysis. As indicated in Table IV, the hybrid detector has provided better performance in terms of P-R than the learning-based methods. The lower performances of the deep-learning-based methods can be linked with the insufficient data for learning at the current stage. However, these performances can be improved with the more data for HSI-based systems as in other detection and classification applications in future.

During the development of the performed research on hyperspectal image surveillance system for explosive detection, the first stage was to collect a spectral library of the targeted explosives with an ASD spectrometer. The list includes about 25 explosives, such as AN, ANFO, TNT, RDX, A4, C3, C4, and others. We observed that most of the spectral signatures of explosives can be categorized into two classes as AN class and RDX class explosives, due to their similar characteristics, especially in the spectral range of 1500–1700 nm. While there is only one dip around 1550 nm for the AN class (AN, NitroMac, and AN compounds, such as ANFO and AN–sugar compound), there are two dips around 1650 nm for the RDX class (RDX, A4, C3, C4, and TNT). Therefore, we selected two representatives as AN and RDX from these explosive materials and designed an experiment that includes both of these explosives. In addition, we should also mention that we have given priority to AN-based explosives in the other experiments, as AN and ANFO was the most frequent explosives encountered in the related events in Turkey.

A question for a general deployment of the proposed system was to reveal the minimum number of bands and the important spectral regions for the performance of detection. Fig. 14 has revealed that the number of bands can be decreased down without a significant loss in recall values. In addition, our experiments on index-based and signature-based methods have indicated that the spectral range of 1500–1700 nm is the most important region that discriminates the explosive, such as AN and RDX, from the background spectra.

A complementary aspect of all the comparisons is the computational complexities of the proposed approaches. Table VI gives the implementation times of the proposed algorithms at a computer with 16 GB RAM and Intel i7-6700 CPU 3.4 GHz. Without loss of generality, the complexity of the index-based method can be regarded as $O(N \times k)$, where N is the number of pixels in the captured HSIs and k is the number of ratios computed for each pixel. The number of ratios is 4 in the proposed algorithm. The computation of the covariance matrix of size $p \times p$ in ACE algorithm has the complexity of $O(N \times p^2)$, where p is the number of spectral bands. Note that the given time in the table also includes the inverse operation for covariance matrix during the implementation. The complexity of matching operation in ACE involves a multiplication of a row vector $(1 \times p)$, a matrix $(p \times p)$, and a column vector $(p \times 1)$ for each pixel. Therefore, its complexity is $O(N \times (p^2 + p))$. The unmixing stage of HSD is computationally the most demanding part among all the algorithms with its complexity $O(N^3)$ [58]. This can also be verified with the given duration in the table. The complexity analysis of deep-learning-based solutions is a challenging task and newly being handled in the related literature [59], [60]. Therefore, we have only sufficed with the number of parameters for the utilized network (as stated in Section II-C) and the duration for the testing of a query HSI in Table VI.

Given the implementation times of the proposed algorithms in Table VI, the index-based method can provide near real-time performances in its current state. However, its detection performances are behind the ACE and HSD. On the other hand, although HSD is the best algorithm in terms of detection performance, it requires further improvement by means of implementation on field programmable gate array (FPGA) and graphics processing units (GPU). The duration of the deep-learning-based method is also not suitable for a practical surveillance system in present form. Considering the ultimate application, the proposed system can be used at static control points to track car bombs for the moment. However, there is still a room for a more generic surveillance system to track the dynamic traffic on specific points of highways.

As the final aspect, considering that the HSD, which combines unmixing and signature-based detection, is the best method among the compared methods, we have also explored whether it can be further improved by means of improving the unmixing part. For this purpose, we have adapted a new unmixing model, namely, augmented linear mixing model (ALMM), to the unmixing part of HSD by means of utilizing the open code shared by the authors of ALMM [61] and then, compared the results. The thresholded score images and the P-R curves presented in Fig. 17 have revealed that the conventional HSD with LMM is giving better results than the ALMM-based solution. While the

TABLE VI
IMPLEMENTATION TIMES OF THE PROPOSED ALGORITHMS

Algorithm	Index based	ACE		HSD		Deep learning
		Covariance estimation	Matching	Unmixing (FCLS)	Matching	Test
Duration (s)	0.056	0.077	0.247	102	0.6	~ 400

(a) (b) (c)

Fig. 17. Thresholded scoremaps for HSD with (a) LMM, (b) ALMM, and (c) precision–recall graphs for both cases.

precision values are very close to each other up to a recall value of about 0.65, the precision of HSD with the ALMM algorithm is getting worse than the one with LMM after this point. The results have emphasized the importance of the unmixing part for the proposed system, which requires more sophisticated analysis in the future. In particular, the best mixing model among alternatives, such as linear mixing model, ALMM, and nonlinear mixing models [62], should be further investigated in future articles.

VI. CONCLUSION

Observing that current methods on HSI methods for explosive detection are mostly tailored for laboratory environments, we first present the challenges for HSI surveillance systems for explosive detection in dynamic scenes in this article. Then, the details of the proposed technical framework from capturing to target detection are given along with the discussions on the performances of different classes of detection methods for various experimental setups including granular explosives, liquid sprayed explosives, and fingerprint residues on vehicle surfaces. The experiments first indicate that the signature-based target detection algorithms yield the best detection performances among three main approaches including index-based and learning-based methods. Considering that the hyperspectral-learning-based methods are still in their initial phase, in particular, for explosive detection, their performances can be improved by further focusing more on training data, new learning strategies, models, and tuning parameters. The index-based methods on the other hand reveal the significance of some specific bands for the detection depending on the chemical structures of the targeted explosives.

Among signature-based target detection methods, the HSD is found superior to its counterparts during the experiments as it first applies unmixing on the pixel spectra and suppresses the effects of the other components during the matching operation in the detector side. The same conclusion has been observed in all designed experiments including solid and sprayed explosive residues. The last experiments on real cases have also indicated that the two explosives on the same surface can be successfully identified from standoff distances by the proposed system. In addition, we have also observed that only 11 short-wave spectral bands are necessary to achieve sufficient detection performances in the tests.

The complexity analysis of the proposed methods has revealed that index-based detection can achieve real-time performances. ACE and HSD methods can also be used for practical systems including static control points. However, the learning-based method requires significant improvements in implementation times. One of the future aspects of the performed research will be the complexity reduction of the utilized approaches. The usage of active sources at control points, the investigation of bidirectional reflectance distribution functions for improved detection, and the extension of the designed experiments for other explosives will be the other aspects that we are planning to focus in further stages of the proposed HSI surveillance system.

Author Contributions: **The overall system design** for hyperspectral image surveillance system for explosive detection is proposed by A.K. and A.A.A. with the contributions of all authors. **The experiments** are designed and prepared by İ.G., M.K., O.B.Ö., and A.K. with the suggestions/contributions of A.A.A., O.E., and Y.Y.Ç. **The data collection** is performed by M.K., İ.G., O.B.Ö., and A.K. **Preprocessing and reflectance conversion** is implemented by M.K. with the suggestions of A.K., A.A.A., O.E., and Y.Y.Ç. **Signature-based target detection methods** are adapted to the proposed surveillance system and implemented by M.K. and supervised by A.K. with the contributions of A.A.A., Y.Y.Ç., and O.E. **The index-based method** for Ammonium Nitrate is developed and implemented by O.B.Ö. with the contributions of O.E. **Learning- and deep-learning-based methods** for the proposed surveillance system are developed and implemented by O.B.Ö. and İ.G. with the contributions of A.K. and A.A.A. **The analysis and interpretation** are performed by all authors at the weekly meetings during the project period. **Manuscript writing** is performed by A.K.,

M.K., O.B.Ö., and İ.G. with the contributions of A.A.A., Y.Y.Ç., and O.E.

REFERENCES

[1] A. Koz, "Ground-based hyperspectral image surveillance systems for explosive detection: Part I—State of the art and challenges," *IEEE J. Sel. Topics Appl. Earth Observ. Remote Sens.*, vol. 12, no. 12, pp. 4746–4753, Dec. 2019.

[2] A. Koz, "Ground-based hyperspectral image surveillance systems for explosive detection: Part II—Radiance to reflectance conversions," *IEEE J. Sel. Topics Appl. Earth Observ. Remote Sens.*, vol. 12, no. 12, pp. 4754–4765, Dec. 2019.

[3] M. J. Khan, H. S. Khan, A. Yousaf, and A. Abbas, "Modern trends in hyperspectral image analysis: A review," *IEEE Access*, vol. 6, pp. 14118–14129, 2018.

[4] P. Yuen and M. Richardson, "An introduction to hyperspectral imaging and its application for security, surveillance and target acquisition," *Imag. Sci. J.*, vol. 58, no. 5, pp. 241–253, 2010.

[5] A. W. Fountain, S. D. Christesen, R. P. Moon, and J. A. Guichetau, "Recent advances and remaining challenges for the spectroscopic detection of explosive threats," *Appl. Spectrosc.*, vol. 68, no. 8, pp. 795–811, Aug. 2014.

[6] L. D. Griffin, M. Caldwell, J. T. A. Andrews, and H. Bohler, "Unexpected item in the bagging area": Anomaly detection in X-ray security images," *IEEE Trans. Inf. Forensics Secur.*, vol. 14, no. 6, pp. 1539–1553, Jun. 2019.

[7] S. Akcay, M. E. Kundegorski, C. G. Willcocks, and T. P. Breckon, "Using deep convolutional neural network architectures for object classification and detection within X-ray baggage security imagery," *IEEE Trans. Inf. Forensics Secur.*, vol. 13, no. 9, pp. 2203–2215, Sep. 2018.

[8] L. A. Skvortsov, "Active spectral imaging for standoff detection of explosives," *Quantum Electron.*, vol. 41, no. 12, pp. 1051–1060, 2011.

[9] R. Ostendorf et al., "Recent advances and applications of external cavity-QCLs towards hyperspectral imaging for standoff detection and real-time spectroscopic sensing of chemicals," *Photonics*, vol. 3, 2016, Art. no. 28.

[10] F. Fuchs et al., "Imaging stand-off detection of explosives using tunable MIR quantum cascade lasers," in *Proc. SPIE 7608, Quantum Sens. Nanophotonic Devices VII*, 2010, Art. no. 760809.

[11] F. Fuchs et al., "Imaging standoff detection of explosives by diffuse reflectance IR laser spectroscopy," in *Future Security. Communications in Computer and Information Science*, N. Aschenbruck, P. Martini, M. Meier, and J. Tölle Eds., vol. 318. Berlin, Germany: Springer, 2012.

[12] B. E. Bernacki and N. Ho, "Differential spectroscopic imaging of particulate explosives residue," in *Proc. SPIE Opt. Photon. Glob. Homeland Secur. IV*, 2008, Art. no. 694517.

[13] B. E. Bernacki and M. C. Philips, "Standoff hyperspectral imaging of explosives residues using broadly tunable external cavity quantum cascade laser illumination," in *Proc. SPIE Chem., Biol., Radiol., Nucl., Explosives Sens. XI*, 2010, Art. no. 76650I.

[14] M. E. Morales-Rodríguez, L. R. Senesac, T. Thundat, M. K. Rafailov, and P. G. Datskos, "Standoff imaging of chemicals using IR spectroscopy," in *Proc. SPIE, Micro- Nanotechnol. Sensors, Syst., Appl. III*, 2011, Art. no. 80312D.

[15] C. S.-C. Yang et al., "Long-wave infrared (LWIR) molecular laser-induced breakdown spectroscopy (LIBS) emissions of thin solid explosive powder films deposited on aluminum substrates," *Appl. Spectrosc.*, vol. 71, no. 4, pp. 1–7, 2017.

[16] J. Macarthur, J. Hayden, M. S. Warden, C. Carson, D. M. Stothard, and V. G. Savitski, "Dual-comb scanning spectrometer for remote sensing of traces of explosives," *IEEE Trans. Instrum. Meas.*, vol. 71, Jan. 2022, Art. no. 7001911.

[17] D. M. Finton, C. J. Breshike, C. A. Kendziora, R. Furstenberg, and R. A. McGill, "Infrared backscatter imaging spectroscopy for standoff detection of hazardous materials," in *Proc. SPIE 12116, Chem., Biol., Radiol., Nucl., Explosives Sens. XXIII*, 2022, Art. no. 121160Q.

[18] C. J. Breshike, C. A. Kendziora, Y. Yoon, R. Furstenberg, V. Nguyen, and R. A. McGill, "Infrared backscatter imaging spectroscopy for standoff detection of trace explosives," in *Proc. SPIE 11010, Chem., Biol., Radiol., Nucl., Explosives Sens. XX*, 2019, Art. no. 1101004.

[19] Y. H. El-Sharkawy and S. Elbasuney, "Hyperspectral imaging: A new prospective for remote recognition of explosive materials," *Remote Sens. Appl.: Soc. Environ.*, vol. 13, pp. 31–38, 2019.

[20] S. Chaudhary, S. Ninsawat, and T. Nakamura, "Non-destructive trace detection of explosives using pushbroom scanning hyperspectral imaging system," *Sensors*, vol. 19, Dec. 2018, Art. no. 97.

[21] K. Ruxton, G. Robertson, W. Miller, G. P. A. Malcolm, and G. T. Maker, "Mid-infrared hyperspectral imaging for the detection of explosive compounds," in *Proc. SPIE 8546, Opt. Photon. Counterterrorism, Crime Fighting, Defense VIII*, May 2012, Art. no. 85460V.

[22] M. Kumar et al., "Stand-off detection of solid targets with diffuse reflection spectroscopy using a high-power mid-infrared supercontinuum source," *Appl. Opt.*, vol. 51, no. 15, pp. 2794–2807, May 2012.

[23] M. P. Nelson, A. Basta, R. Patil, O. Klueva, and P. J. Treado, "Development of a handheld widefield hyperspectral imaging (HSI) sensor for standoff detection of explosive, chemical, and narcotic residues," in *Proc. SPIE 8726Next-Gener. Spectrosc. Technol. VI*, 2013.

[24] B. M. Onat, G. Carver, and M. Itzler, "A solid-state hyperspectral imager for real-time standoff explosives detection using shortwave infrared imaging," in *Proc. SPIE 7310 Non-Intrusive Inspection Technol. II*, 2009, Art. no. 731004.

[25] T. A. Blake, J. F. Kelly, N. B. Gallagher, P. L. Gassman, and T. J. Johnson, "Passive standoff detection of RDX residues on metal surface via infrared hyperspectral imaging," *Anal. Bioanal. Chem.*, vol. 395, pp. 337–348, Sep. 2009.

[26] A. L. Bingham, P. G. Lucey, J. T. Akagi, J. L. Hinrichs, and E. T. Knobbe, "LWIR hyperspectral micro-imager for detection of trace explosive particles," in *Proc. SPIE 9101 Next-Gener. Spectrosc. Technol. VII*, May 2014, Art. no. 91010Z.

[27] M. A. F. de la Ossa, J. M. Amigo, and C. G. Ruiz, "Detection of residues from explosive manipulation by near infrared hyperspectral imaging: A promising forensic tool," *Forensic Sci. Int.*, vol. 242, pp. 228–235, 2014.

[28] A. Abdallah, A. Mokhtar, H. S. Ayoub, and Y. H. Elbashar, "Experimental study on standoff detection of explosives traces using Laser Raman spectroscopy: Challenges and possible solution," *Opt. Quantum Electron.*, vol. 54, 2022, Art. no. 345.

[29] D. Avola, M. Cascio, L. Cinque, A. Fagioli, and C. Petrioli, "Person re-identification through Wi-Fi extracted radio biometric signatures," *IEEE Trans. Inf. Forensics Secur.*, vol. 17, pp. 1145–1158, Mar. 2022.

[30] Y. Cong, J. Yuan, and Y. Tang, "Video anomaly search in crowded scenes via spatio-temporal motion context," *IEEE Trans. Inf. Forensics Secur.*, vol. 8, no. 10, pp. 1590–1599, Oct. 2013.

[31] U. Park, H. -C. Choi, A. K. Jain, and S. -W. Lee, "Face tracking and recognition at a distance: A coaxial and concentric PTZ camera system," *IEEE Trans. Inf. Forensics Secur.*, vol. 8, no. 10, pp. 1665–1677, Oct. 2013.

[32] F. Mokhayeri, E. Granger, and G.-A. Bilodeau, "Domain-specific face synthesis for video face recognition from a single sample per person," *IEEE Trans. Inf. Forensics Secur.*, vol. 14, no. 3, pp. 757–772, Mar. 2019.

[33] H. Su, H. Yang, S. Zheng, Y. Fan, and S. Wei, "The large-scale crowd behavior perception based on spatio-temporal viscous fluid field," *IEEE Trans. Inf. Forensics Secur.*, vol. 8, no. 10, pp. 1575–1589, Oct. 2013, doi: 10.1109/TIFS.2013.2277773.

[34] N. Pettorelli, *The Normalized Difference Vegetation Index*. Oxford, U.K.: Oxford Univ. Press, 2013.

[35] G. Bo-Cai, "NDWI—A normalized difference water index for remote sensing of vegetation liquid water from space," *Remote Sens. Environ.*, vol. 58, no. 3, pp. 257–266, 1996.

[36] H.-Q. Xu, "A study on information extraction of water body with the modified normalized difference water index (MNDWI)," *J. Remote Sens.*, vol. 5, pp. 589–595, Sep. 2005.

[37] S-N. Haubrock, C. Sabine, C. Lemmnitz, and H. Kaufmann, "Surface soil moisture quantification models from reflectance data under field conditions," *Int. J. Remote Sens.*, vol. 29, pp. 3–29, 2008.

[38] D. Yingbin, C. Wu, M. Li, and R. Chen, "RNDSI: A ratio normalized difference soil index for remote sensing of urban/suburban environments," *Int. J. Appl. Earth Observ. Geoinf.*, vol. 39, pp. 40–48, 2015.

[39] N. M. Nasrabadi, "Hyperspectral target detection," *IEEE Signal Process. Mag.*, vol. 31, no. 1, pp. 34–44, Jan. 2014.

[40] X. Jin, S. Paswaters, and H. Cline, "A comparative study of target detection algorithms for hyperspectral imagery," in *Proc. SPIE*, 2009, Art. no. 73341W.

[41] M. T. Eismann, "Hyperspectral target detection," in *Hyperspectral Remote Sensing*, chapter 14. Bellingham, WA, USA, SPIE Press, 2012, pp. 646–716.

[42] E. Truslow, "Performance evaluation of the adaptive cosine estimator detector for hyperspectral imaging applications," M.S. thesis, Dept. Elect. Comput. Eng., Northeastern Univ., Boston, MA, USA, Aug. 2012.

[43] O. L. Frost, "An algorithm for linearly constrained adaptive array processing," *Proc. IEEE*, vol. 60, no. 8, pp. 926–935, Aug. 1972.
[44] H. Ren and C.-I Chang, "Automatic spectral target recognition in hyperspectral imagery," *IEEE Trans. Aerosp. Electron. Syst.*, vol. 39, no. 4, pp. 1232–1249, Oct. 2003.
[45] J. Broadwater and R. Chellappa, "Hybrid detectors for subpixel targets," *IEEE Trans. Pattern Anal. Mach. Intell.*, vol. 29, no. 11, pp. 1891–1903, Nov. 2007.
[46] D. Heinz, C.-I Chang, and M. L. G. Althouse, "Fully constrained least-squares based linear unmixing," in *Proc. IEEE Geosci. Remote Sens. Symp.*, 1999, pp. 1401–1403.
[47] L. E. Christovam, G. G. Pessoa, M. H. Shimabukuro, and M. L. B. T. Galo, "Land use and land cover classification using hyperspectral imagery: Evaluating the performance of spectral angle mapper, support vector machine and random forest," *Int. Arch. Photogrammetry, Remote Sens. Spatial Inf. Sci.*, vol. XLII-2/W13, pp. 1841–1847, 2019.
[48] U. B. Gewali, S. T. Monteiro, and E. Saber, "Machine learning-based hyperspectral image analysis: A survey," 2019, *arXiv:1802.08701*.
[49] R. Heylen, M. Parente, and P. Gader, "A review of nonlinear hyperspectral unmixing methods," *IEEE J. Sel. Topics Appl. Earth Observ. Remote Sens.*, vol. 7, no. 6, pp. 1844–1868, Jun. 2014.
[50] Y. Radhika and M. Shashi, "Atmospheric temperature prediction using support vector machines," *Int. J. Comput. Theory Eng.*, vol. 1, no. 1, pp. 55–58, Apr. 2009.
[51] G. Moser and S. B. Serpico, "Automatic parameter optimization for support vector regression for land and sea surface temperature estimation from remote sensing data," *IEEE Trans. Geosci. Remote Sens.*, vol. 47, no. 3, pp. 909–921, Mar. 2009.
[52] Y. Li, H. Zhang, and Q. Shen, "Spectral–spatial classification of hyperspectral imagery with 3D convolutional neural network," *Remote Sens.*, vol. 9, no. 1, 2017, Art. no. 67.
[53] H. Lee and H. Kwon, "Going deeper with contextual cnn for hyperspectral image classification," *IEEE Trans. Image Process.*, vol. 26, no. 10, pp. 4843–4855, Oct. 2017.
[54] A. Ben Hamida, A. Benoit, P. Lambert, and C. Ben Amar, "3-D deep learning approach for remote sensing image classification," *IEEE Trans. Geosci. Remote Sens.*, vol. 56, no. 8, pp. 4420–4434, Aug. 2018.
[55] D. Hong, L. Gao, J. Yao, B. Zhang, A. Plaza, and J. Chanussot, "Graph convolutional networks for hyperspectral image classification," *IEEE Trans. Geosci. Remote Sens.*, vol. 59, no. 7, pp. 5966–5978, Jul. 2021.
[56] D. Hong et al., "More diverse means better: Multimodal deep learning meets remote-sensing imagery classification," *IEEE Trans. Geosci. Remote Sens.*, vol. 59, no. 5, pp. 4340–4354, May 2021.
[57] X. Wu, D. Hong, and J. Chanussot, "UIU-Net: U-Net in U-Net for infrared small object detection," *IEEE Trans. Image Process.*, vol. 32, pp. 364–376, Dec. 2022.
[58] C. Puladas, K. Hossler, and J. N. Ash, "Sum-product unmixing for hyperspectral analysis with endmember variability," *IEEE Geosci. Remote Sens. Lett.*, vol. 15, no. 12, pp. 1917–1921, Dec. 2018.
[59] X. Hu et al., "Model complexity of deep learning: A survey," *Knowl. Inf. Syst.*, vol. 63, pp. 2585–2619, 2021.
[60] T. Kam Ho, "Complexity of representations in deep learning," in *Proc. IEEE 26th Int. Conf. Pattern Recognit.*, 2022, pp. 2657–2663.
[61] D. Hong, N. Yokoya, J. Chanussot, and X. X. Zhu, "An augmented linear mixing model to address spectral variability for hyperspectral unmixing," *IEEE Trans. Image Process.*, vol. 28, no. 4, pp. 1923–1938, Apr. 2019.
[62] O. B. Özdemir, A. Koz, and Y. Y. Çetin, "Non-linear hyperspectral unmixing with 3D convolutional encoders," *Int. J. Remote Sens.*, vol. 43, pp. 3236–3257, 2022.

Mustafa Kütük received the B.S. degree in electrical and electronics engineering and the Double Major degree in computer engineering from the Dokuz Eylül University, Izmir, Turkey, in 2014, and the M.S. degree in electrical and electronics engineering in 2018 from the Middle East Technical University (METU), Ankara, Turkey, where he is currently working toward the Ph.D. degree in the scientific computing program with the Institute of Applied Mathematics.

From 2016 to 2019, he was a Researcher with the Center for Image Analysis, METU. Since 2019, he has been a Research Assistant with the Scientific Computing program, Institute of Applied Mathematics, METU. His research interests include deep learning, hyperspectral image analysis, image processing, and scientific machine learning.

İzlen Geneci received the B.S. degree in electrical and electronics engineering from the Bilkent University, Ankara, Turkey, in 2016, and the M.S. degree in cognitive science from the Middle East Technical University (METU), Ankara, Turkey, in 2022.

She conducted research with the Center for Image Analysis, METU, from 2016 to 2021. She joined the Turkey's Automobile Joint Venture Group Inc., in 2021. Her research interests include deep learning, computer vision, hyperspectral image analysis, and audio processing.

Okan Bilge Özdemir received the M.S. and Ph.D. degrees in information systems from the Middle East Technical University, Ankara, Turkey, in 2013 and 2021, respectively.

He has been an Assistant Professor with the Department of Computer Engineering, Artvin Çoruh University, Artvin, Turkey, since 2022. He is currently performing postdoctoral research studies with the Cedars Sinai Medical Center, Los Angeles, CA, USA. His research interests include deep learning, image processing, hyperspectral image analysis, and medical image processing.

Alper Koz was born in Kahramanmaras, Turkey, in 1978. He received the B.S., M.S., and Ph.D. degrees in electrical and electronics engineering from the Middle East Technical University (METU), Ankara, Turkey, in 2000, 2002, and 2007, respectively.

He performed postdoctoral research studies with the Multimedia Signal Processing Laboratory, Delft University of Technology, Delft, The Netherlands, from 2008 to 2010; with the Laboratory Signals and Systems, SUPELEC, Paris, France, from 2010 to 2011; and with the Multimedia Group of Telecom ParisTech, Paris, France, from 2011 to 2013. He joined the Center for Image Analysis, METU, in 2014. His research interests include hyperspectral image analysis, high dynamic range image and video processing, and multimedia watermarking and fingerprinting.

Dr. Koz is an Associate Editor for *Elsevier Signal Processing: Image Communication*.

Okan Esentürk received the B.S. degree in chemistry from the Middle East Technical University (METU), Ankara, Turkey, in 1996, and the Ph.D. degree in chemistry from the University of Maryland, College Park, MD, USA, in 2004.

Since 2009, he has been a Professor with the Department of Chemistry, Middle East Technical University (METU). He was a Postdoctoral Fellow and then a Guest Researcher with the National Institute of Standard and Technology between 2004 and 2009 and worked under the guidance of Edwin J. Heilweil. His research interests include spectroscopy in hyperspectral imaging, light and matter interaction for better the understanding of the chemical characteristics of materials, determination dielectric properties of the materials in terahertz range, development of new methods and/or techniques based on spectroscopy for nondestructive testing of materials, ultrafast laser spectroscopy, and the study of photoconductivity with THz spectroscopy.

Yasemin Yardımcı Çetin received the B.S. and M.S. degrees from the Bogazici University, Istanbul, Turkey, in 1983 and 1988, respectively, and the Ph.D. degree from the Vanderbilt University, Nashville, TN, USA, in 1994, all in electrical engineering.

After working as a Postdoctoral Associate and Part-Time Teacher at various institutions, including the Bogazici University, Bilkent University, University of Minnesota, and Middle East Technical University (METU), she joined METU as a Permanent Faculty with Informatics Institute. She held a number of administrative positions with the METU and the local IEEE Section. She was the Director of the Modeling and Simulation Center and served as the Department Head of Information Systems when she retired. She is currently an Adjunct Faculty with the University of Illinois, Chicago, IL, USA, and also the owner of a startup ZQAI LLC. Her research interests include hyperspectral imaging and machine learning.

A. Aydın Alatan was born in Ankara, Turkey, in 1968. He received the B.S. degree in electrical engineering from the Middle East Technical University, Ankara Turkey, in 1990, the M.S. and DIC degrees in electrical engineering from the Imperial College of Science, Medicine and Technology, London, U.K., in 1992, and the Ph.D. degree in electrical engineering from the Bilkent University, Ankara, Turkey, in 1997.

He was a Postdoctoral Research Associate with the Center for Image Processing Research, Rensselaer Polytechnic Institute, Troy, NY, USA, between 1997 and 1998, and with the New Jersey Center for Multimedia Research, New Jersey Institute of Technology, New Jersey, NJ, USA, between 1998 and 2000. In 2000, he joined as a Faculty of Electrical and Electronics Engineering Department with the Middle East Technical University. He is the Founding Director for the Center for Image Analysis.

Dr. Alatan is a member of The Science Academy of Turkey.